Broadband Subwavelength Imaging Using a Tunable Graphene-Lens

Peining Li and Thomas Taubner*

1st Institute of Physics (IA), RWTH Aachen University, 52056 Aachen, Germany

ABSTRACT Graphene as a one-atom-thick planar sheet can support surface plasmons at infrared (IR) and terahertz (THz) frequencies, opening up exciting possibilities for the emerging research field of graphene plasmonics. Here, we theoretically report that a layered graphene-lens (GL) enables the enhancement of evanescent waves for near-field subdiffractive imaging. Compared to other resonant imaging devices like superlenses, the nonresonant operation of the GL provides the advantages of a broad intrinsic bandwidth and a low sensitivity to losses, while still maintaining a good subwavelength resolution of better than $\lambda/10$. Most importantly, thanks to the large tunability of the graphene, we show that our GL is a continuously frequency-tunable subwavelength-imaging device in the IR and THz regions, thus allowing for ultrabroadband spectral applications.

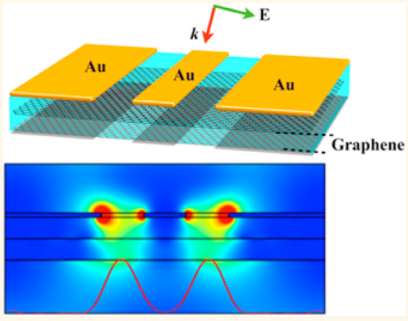

KEYWORDS: subwavelength imaging · graphene · frequency-tunable · broadband · loss-insensitivity

Imaging with a resolution beyond the diffraction limit has been always one of the most important issues in the field of optics, since Ernst Abbe[1] discovered this fundamental barrier in 1873. The loss of subwavelength features of objects due to the fast decay of evanescent waves limits the resolution of a classical imaging system to about half of the illuminating wavelength. To overcome this limitation and recover fine details of objects, one fundamental idea is to enhance and detect evanescent waves in the near field.[2−5] For example, in scanning near-field optical microscopy (SNOM) a sharp tip is used to produce strong local field enhancement and simultaneously collect near-field information of samples.[4−10] This enhancement is usually a nonresonant effect, thus independent of the radian frequency allowing for nanoscale-resolution imaging at frequencies ranging from the visible[6] to the THz regime.[7] With this frequency-independence the SNOM can be used for many spectroscopic applications, such as characterization of free-carrier concentrations of doped semiconductors,[7] vibrational spectroscopy,[8,9] and organic structure identification.[10] However, the high spatial resolution in SNOM comes at the price of a pixel-by-pixel scanning of the tip close to the sample. This obvious time-consuming characteristic restricts its application to small-area samples (typically 10 μm $\times$ 10 μm or even less) for imaging within reasonable time. For the demand of rapid and large-area sample detecting at high spatial resolution, other methods are needed.

A major step toward this goal is a recently developed device known as a superlens (SL) that is capable of imaging the samples at subwavelength resolution by using a thin slab of a material with negative permittivity.[2,3,11−16] In principle, due to the small effective wavelength of surface modes at the interfaces between the negative-permittivity layer and positive-permittivity host, the SL can be seen as a practical version of perfect lens[2] allowing for nondiffraction-limited imaging and sensing. Particularly, unlike the tip-based SNOM, the SL is a planar imaging device that allows for rapidly probing large-area samples, which leads to new superlens-based nanolithography.[16] However, a new emerging limitation in the SL is the narrow working-frequency range. Although the surface resonance contributes a lot to the ultrahigh resolution of the SL, it also constrains that the SL can only work in the frequency range close to the resonance,[12−14] which limits superlenses in spectroscopic applications. Recently, it has been shown that exploiting a series of various superlenses[13,14] or a multifrequency SL[15] with different phonon resonances can

* Address correspondence to taubner@physik.rwth-aachen.de.

Received for review August 22, 2012 and accepted October 9, 2012.

Published online October 09, 2012
10.1021/nn303845a

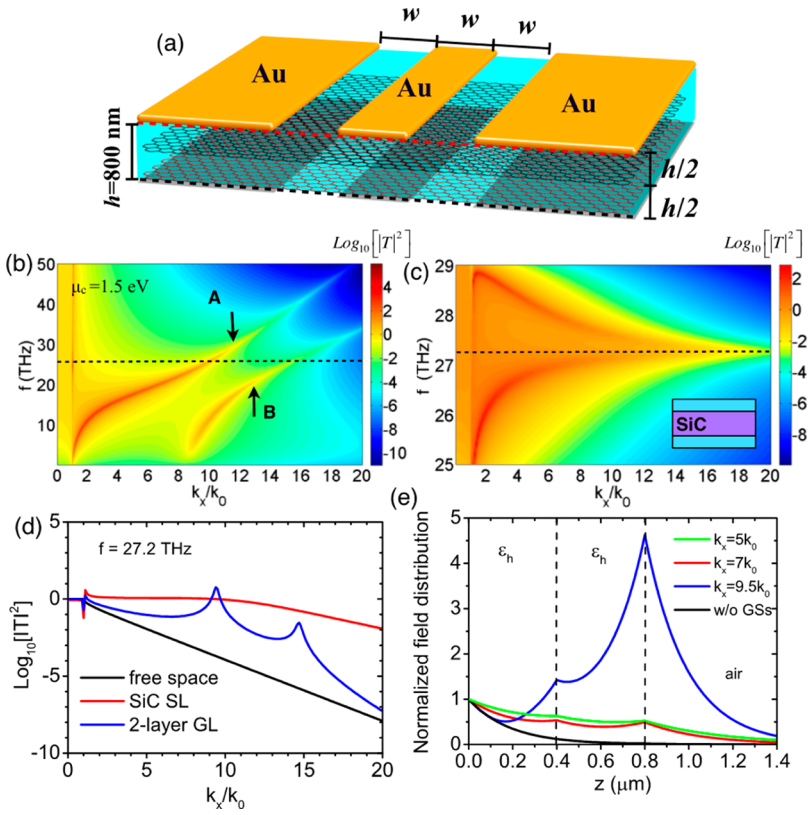

Figure 1. Comparison of the OTF of the 2-layered GL and the SiC SL. (a) Sketch of a 2-layered GL under the Au double slit. The red and black dashed lines indicate the positions of object plane and image plane chosen for later numerical simulations. (b) The calculated spectral OTF of a 2-layered GL with the thickness of 800 nm under the applied chemical potential $\mu_c = 1.5$ eV. (c) The spectral OTF of a typical SL with the material combination of SiC and SiO_2. (d) Comparison of the OTF for those two cases in panels b and c at the same frequency $f = 27.2$ THz. (e) Calculated electric field distribution for different evanescent components through the 2-layered GL with $\mu_c = 1.5$ eV: $k_x = 5k_0$ (light green), $7k_0$ (red) and $9.5k_0$ (blue). The black dashed lines indicate the positions of the GSs. For comparison, the case without the GSs (black) is also shown in the same figure.

be a reasonable route to broaden the covered frequency range, but in these setups there will be large gaps between multiple resonant frequencies that cannot be filled up yet.

Here we propose that a novel frequency-tunable graphene-lens can achieve subdiffractive imaging with an ultrabroad covered frequency range. Recently, it has been demonstrated that graphene sheets (GSs) can support[17−21] and guide[22] surface plasmons with ultrashort effective wavelength for potential metamaterial and plasmonic applications.[23−30] In this theoretical study, we verify that well-coupled GSs also enable the enhancement of evanescent waves for subwavelength imaging. Owing to the nonresonant nature of the imaging process, this enhancement is obviously weaker than the superlensing effect, but still a good subwavelength resolution of around $\lambda/7$ can be achieved for a bilayer case, and can be further improved to better than $\lambda/10$ *via* multilayered configuration. More importantly, due to the advantage that the complex conductivity of graphene can be controlled with variations of chemical potential by external ways (gate voltage,[31] electric field,[32,33] and/or chemical doping[34]), the working frequency of the GL can be continuously tuned in the range of IR and THz frequencies, effectively broadening the total working frequency range.

RESULTS

Enhancing Evanescent Waves for Subwavelength Imaging. The key process in the GL concept is the nonresonant enhancement of evanescent waves. To show this important effect, we start with a bilayer GL as illustrated in Figure 1a, where two GSs are embedded in a host dielectric medium with a permittivity of $\varepsilon_h = 3$. The total thickness of the GL is $h = 800$ nm. In this work, we suppose that each graphene layer has the same complex conductivity ($\sigma_g = \sigma_1 + i\sigma_2$), which relates with radian frequency ω, operation temperature T, chemical potential μ_c, and relaxation time τ. A general expression of σ_g determined from the Kubo formula is obtained as[28,34,35]

$$\sigma_g = \frac{e^2(\omega + i\tau^{-1})}{i\hbar}\left[\frac{1}{(\omega+i\tau^{-1})^2}\int_0^\infty \varepsilon\left(\frac{\partial F(\varepsilon)}{\partial \varepsilon} - \frac{\partial F(-\varepsilon)}{\partial \varepsilon}\right)d\varepsilon - \int_0^\infty \frac{\partial F(-\varepsilon) - \partial F(\varepsilon)}{(\omega+i\tau^{-1})^2 - 4(\varepsilon/\hbar)^2}\,d\varepsilon\right] \quad (1)$$

where $F(\varepsilon) = (1 + \exp[(\varepsilon - \mu_c)/K_BT])^{-1}$ is the Fermi−Dirac distribution, ε is the energy, and $\hbar$ is reduced Plank's constant. In this paper, all the examples are supposed to

work at room temperature considering practical application prospects.

The optical transfer function (OTF),[36] which is the transmittance $|T|^2$ through the device as a function of the frequency f and wave vector k_x, is a established method to evaluate the enhancement of evanescent waves, because both the dispersion relation and transmission properties of the investigated system can be clearly presented at the same time. In Figure 1b, we calculate spectral OTF of the bilayer GL by treating graphene layers as ideal conducting sheets with surface conductivity σ_g (see Methods). First, we simply choose the chemical potential $\mu_c = 1.5$ eV. The relaxation time is set as $\tau = 0.5$ ps, which is a reasonable value consistent with the experimental observation.[36] For comparison, in Figure 1c we also show the OTF of a $SiO_2-SiC-SiO_2$ SL[12] with the same total thickness of 800 nm. Very different dispersive properties are found in these two cases. In the superlensing effect, two transmission modes approach and merge at the frequency possessing extraordinary transmission of evanescent waves. In contrast, for the GL two transmission modes (A and B in Figure 1b) are also exited, but will not combine at a particular frequency because of geometric symmetry breaking (*i.e.*, GSs nonsymmetrically inserted into the dielectric layer, see the Supporting Information). Consistent with the findings in ref 38, these two modes have different physical origins. The first peak A corresponds to the surface mode located on each graphene sheet. And the peak B results from Fabry–Perot resonances—standing waves between graphene layers, which can be controlled by the number of graphene layers as shown in the Supporting Information.

Moreover, in Figure 1b a significant enhanced transmission (warm colors) is also observed in this GL at very high spatial frequencies, indicating the enhancement of evanescent fields. To better show this performance, we compare optical transfer functions of the double-layer GL, the SiC-SL and the case of free space at the same frequency $f = 27.2$ THz (≈ 11 μm, the resonance of the SiC-SL) in Figure 1d. It is clearly seen that in free space the transmittance of subwavelength components decays very fast. On the other hand, in the SiC-SL the transmittance for all evanescent waves is uniformly amplified due to the resonant nature of surface modes at the matching $SiC-SiO_2$ interface, leading to nearly perfect imaging in the near field. Interestingly, the bilayer GL is an intermediate case between the SL and the case of free space. For example, for $k_x = 8k_0$, $|T_{bare}| = 0.02 < |T_{GL}| = 0.3 < |T_{SL}| = 0.9$. Practically, this nonresonant enhancement ($|T_{GL}|/|T_{bare}| = 15$) can already enable near-field applications. For example, in the SNOM the probing tip can also detect weak evanescent fields emerging from structures buried below a surface, as demonstrated recently in subsurface imaging.[39,40] Combining the GL with the SNOM, this capability will be dramatically improved by a further enhancement of the evanescent field, and thus yield a significant increase in sensitivity and resolution.

For the possibility of near-field imaging, we notice that the enhanced transmission curve ($|T| > 0.25$) stays relatively smooth and flat in the range before approaching the first peak A ($k_x \leq 8k_0$), which means that evanescent fields in this range can be effectively transferred through the GL avoiding the signal distortion.[41] To better understand this nearly uniform enhancement, we calculate the electric field distributions for different subwavelength components through the GL as shown in Figure 1e. It is easily seen that all these components are enhanced due to the presence of GSs, and the strongest enhancement is obtained at the position of peak A ($k_x = 9.5k_0$). Intuitively, one could assume that the larger the evanescent fields are, the better the subwavelength resolution would be. However, the strong field amplification at $k_x = 9.5k_0$ is not useful for subdiffractive imaging because of the creation of propagating surface waves, thus distorting the image. For the components of $k_x \leq 8k_0$, the field enhancement is more uniform, which suggests a possibility of subwavelength imaging with a resolution in this spatial frequency range.

Performance of near-Field Subwavelength Imaging. To demonstrate the imaging ability of the suggested GL, we perform numerical simulations using a commercial software based on the finite element method (see Methods). In these simulations, the bilayer GL is used to image a typical resolution-testing pattern: an Au double slit. As sketched in Figure 1a, the double slit with the width $w = 800$ nm is on the dielectric layer of the GL. The center-to-center separation of the slit is chosen to be $2w = 1.6$ μm. For the sake of simulations (see Methods), we treat graphene layers as thin metal layers with the corresponding equivalent permittivity ε_{eq} by following the same method described in literature.[25,28]

The simulated intensity distribution of the total electric field at $f = 27.2$ THz is illustrated in Figure 2a. The electric fields through each slit are effectively transferred (without obvious decreases) by the GL, and thus the slits are also easily distinguished. From the line profile at the image plane shown in Figure 2b, two well-separated peaks are clearly resolved for the case of the double slit on the GL, showing an improved subwavelength resolution ($\sim\lambda/7$) compared with the case without the GL. Furthermore, we also show the performance of this GL at different frequencies in the same figure. The double slit can be resolved by the GL in the range from 26 to 30 THz, suggesting an intrinsic operating frequency range of at least 4 THz. Obviously, the good performance of operation bandwidth of the GL will provide more convenience in future practical applications, such as spectroscopic imaging or near-field lithography without exactly matching the frequency.

Tuning and Loss Effects. From the results of numerical simulations, we have proven that the proposed GL can

achieve subwavelength imaging with a resolution of around $\lambda/7$ in a relatively wide frequency range for a constant chemical potential (or surface conductivity). This covered frequency range can be also directly obtained in the calculation of the OTF. As shown in Figure 3a, the transmittance of the component $k_x = 7k_0$ is plotted as a function of the frequency f for the cases of the GL and the SL. The frequency range obtained from the numerical simulations corresponds to the transmittance within the range $0.1 \leq |T| \leq 0.32$, roughly determining the condition where this GL can achieve subwavelength imaging. On the basis of this condition, we will present the possibility of tuning the imaging frequencies of the GL by changing chemical potentials.

In Figure 3b, we show the contour plot of the transmittance as a function of the chemical potential μ_c and frequency f. In principle, the imaging frequency range (marked with oblique lines) of the GL can be continuously tuned from mid-IR to THz frequencies when we decrease the chemical potential from 1.5 to 0.1 eV. For example, the frequency corresponding to

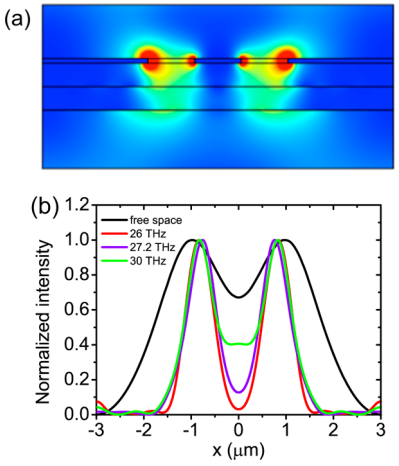

Figure 2. Imaging performance of the 2-layered GL. (a) Electric-field intensity distribution for the case using the 2-layered GL to image an Au double slit with the width w = 800 nm and the separation of $2w$ = 1.6 μm at the frequency f = 27.2 THz. (b) Line profiles taken from the image plane at different frequencies: f = 26 THz (red), 27.2 THz (purple), and 30 THz (green). The case without the GL (black) is shown for comparison.

$|T| = 0.3$ (for $k_x = 7\ k_0$) will shift from 27.2 THz to 13 THz when we change the μ_c from 1.5 to 0.2 eV. We also notice that the bandwidth of the GL will be broadened when it is tuned to work at lower frequencies. For the chemical potential μ_c = 0.2 eV, the covered range of the GL is about 8 THz wide, from 12 to 20 THz. This better performance of the bandwidth at low frequencies is because the GL is becoming "thinner" compared to the operating wavelength, providing higher and more uniform transmission properties. In previous discussions, we just simply choose the chemical potential of the graphene as μ_c = 1.5 eV for comparison with the SiC-SL. However, a reasonable tuning range of the chemical potential is limited to $\mu_c \leq 1.2$ eV based on the current situation that a carrier density of up to 10^{14} cm^{-2} has been realized in experiments.[42,43] Therefore, as seen from Figure 3b, the operating frequencies of our 2-layered GL are covering the range from 28 THz (maximum covered frequency at μ_c = 1.2 eV) to 8 THz (minimum covered frequency at μ_c = 0.1 eV). With this large tunability of imaging frequencies, our bilayer GL can definitely act as an ultrabroadband subdiffractive imaging system at IR and THz regimes.

In addition to the large tunability, we have also investigated the impact of material loss on the performance of the GL. The losses of our system may come from two different parts: the graphene and dielectric layers. According to very recent experiments of SNOM mapping of graphene surface-plasmons, both parts of losses can limit the performance of upcoming graphene-based plasmonic devices: in ref 19, a small mobility of 1200 cm^2 V^{-1} s^{-1} resulted in high intrinsic graphene losses while in ref 20 a faster mobility of 8000 cm^2 V^{-1} s^{-1} was attributed but IR losses of the SiO_2 substrate occurred. For the graphene, the momentum relaxation time τ indicates the level of the loss. Shorter relaxation time means larger scattering loss. In the first part of our work, we just discussed a GL with a small loss: the relaxation time in graphene is τ = 0.5 ps (corresponding to a mobility of about 15 000 cm^2 V^{-1} s^{-1}) and the dielectric layer is lossless. Now we will discuss the situation of the GL with large losses. In Figure 4a, we recalculate the spectral OTF of the

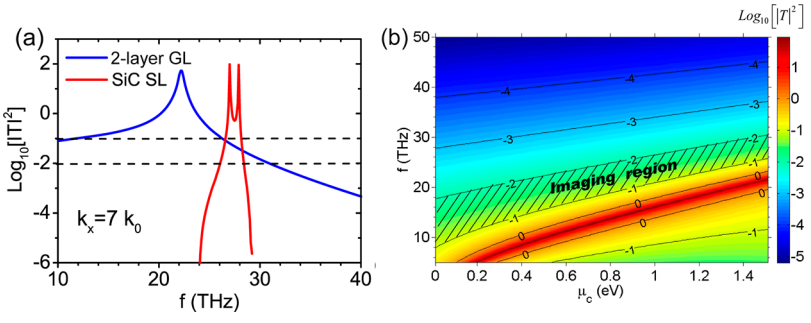

Figure 3. Tuning dependence on the chemical potential and radian frequency. (a) The transmittance of the component k_x = $7k_0$ as a function of the frequency f for the cases of the GL (blue) and the SL (red). (b) Contour plot of the transmittance of the GL as a function of the chemical potential and frequency. The imaging region is the green area marked with oblique lines.

2-layered GL by taking into account a large loss from both graphene (τ = 0.05 ps for a mobility of about 1500 $cm^2\ V^{-1}\ s^{-1}$) and host material (Im[ε_h] = 0.3). At this case two transmission modes A and B (discussed in Figure 1b) are suppressed due to the large loss, and the Fabry–Perot mode even totally disappears at this case. Interestingly, we notice that the transmission of evanescent components in the spatial frequency range of interest ($k_x \leq 8k_0$) is not as sensitive to the loss and still maintains relatively large values. As shown in Figure 4b, the transmission in this range does not change so much for different losses cases: the small loss, the reasonable loss (τ = 0.3 ps for a mobility of about 8000 $cm^2\ V^{-1}\ s^{-1}$ and Im[ε_h] = 0.3), and the large loss. This loss-insensitivity means that the imaging performance of our GL will not be obviously affected by the loss, which is another important property for future practical applications.

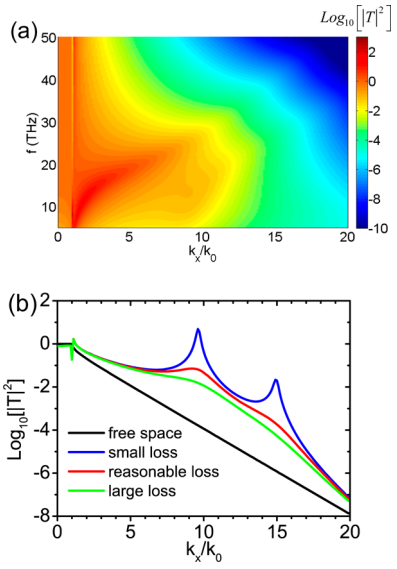

Figure 4. Effect of loss on the GL. (a) Spectral OTF of a 2-layered GL with large losses (τ = 0.05 ps and Im[ε_h] = 0.3) under the applied chemical potential μ_c = 1.5 eV. (b) Comparison of the OTF for three cases with a small loss, a reasonable loss, and a large loss at the frequency *f* = 27.2 THz.

Multilayered Graphene Operation. As above-discussed, higher imaging frequencies require larger chemical potentials in our GL. Decreasing the operating temperature of the system might lower the requirement of chemical potentials,[25] but will introduce some inconveniences compared to the case working at room temperature. Here we extend the GL to multilayer operation by adding more GSs and shortening the distance between two neighbor graphene layers, which also help our device to cover higher frequencies with lower chemical potentials. To demonstrate this idea, we choose the cases of 4-layered GL and 8-layer GL as the examples, while keeping the total thickness of each system to 800 nm constant for comparison. The separation of GSs is reduced to 200 nm for the 4-layer GL and 100 nm for the 8-layer GL. In Figure 5a,b, we show the OTF for these two cases with relatively low chemical potentials: μ_c = 1 eV for the 4-layer GL and μ_c = 0.6 eV for 8-layer GL. Similar with the results of the bilayer GL, obviously large transmission of evanescent components is also found in both multilayered cases

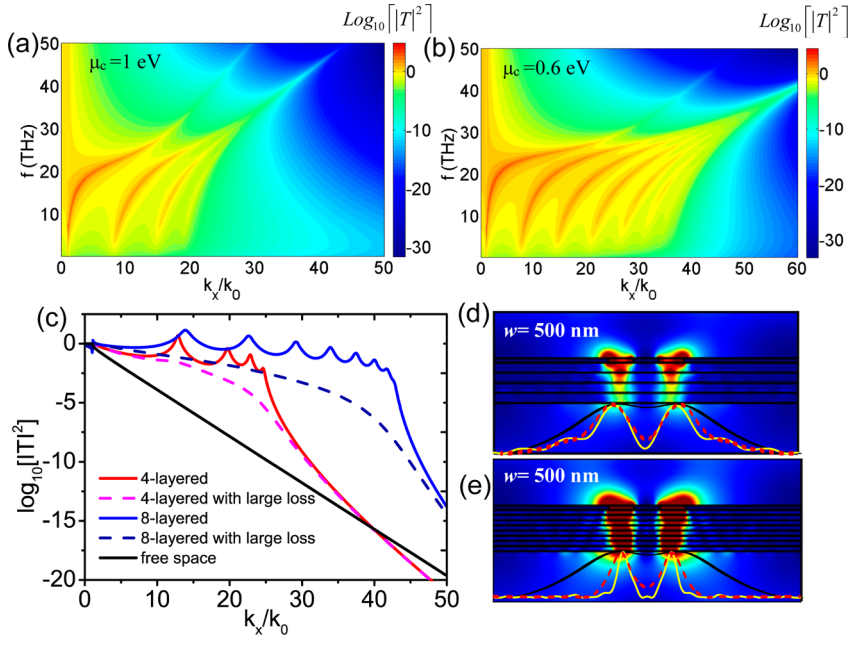

Figure 5. Performance of the multilayered GL. Spectral OTF of multilayered graphene lenses: (a) 4-layered GL with μ_c = 1 eV and (b) 8-layered GL with μ_c = 0.6 eV. (c) Comparison of the OTF for the 4-layered GL and 8-layered GL with different losses at the frequency *f* = 27.2 THz. Electric-field intensity distribution for the cases of (d) 4-layered GL and (e) 8-layered GL at 27.2 THz. Line profiles of intensity distribution at the image plane for the cases of graphene lenses with different losses: small losses (yellow solid lines) and large losses (red dashed lines). The case without the GL (black) is shown for comparison.

(detailed examination shown in Figure 5c), which strongly demonstrates that a multilayered GL can enhance evanescent waves with low chemical potential.

These results can be easily understood by considering the addition of extra GSs. In the bilayer GL case, only two GSs contribute to the enhancement of evanescent waves. Effectively transferring subwavelength information between these two sheets with a large separation of 400 nm requires the large surface conductivity (or chemical potential) in each layer. Here when the GL is extended to the multilayered configuration, more graphene layers with smaller separations can also provide the same enhancing effect of evanescent waves. Therefore, the average enhancement of each graphene layer is lower than that of 2-layered case, resulting in the lower requirement of chemical potential in each sheet.

Another consequence of the multilayered configuration is the improved resolution. As discussed before, the resolution of the GL is limited by surface plasmons on the GSs. Narrowing the separation of graphene layers can lead them to support surface modes with smaller wavelength, resulting in the improvement of resolutions. As seen in Figure 5c, for both multilayered cases the first transmission peaks consisting of coupled surface modes shift to higher spatial frequency. For instance, for the 4-layered case the peak shifts to about $k_x = 14\,k_0$ and $k_x = 17\,k_0$ for the 8-layered case. Therefore, their resolutions are improved to over $\lambda/10$. In principle, the smaller the graphene-period is in the multilayered GL, the better resolution it can achieve. For an example of an 80-layered GL (the layer separation is 10 nm) at $f = 27.2$ THz, the resolution can be further improved to a value of better than $\lambda/50$. In an extreme situation that the separation between the GSs is reduced to match the realistic thickness of the graphene layer, the multilayered GL can work as a multilayered graphene-based SL at ultraviolet (UV) frequency, which is very similar with a recent proposal of an ultraviolet graphene-based hyperlens[29] (We have to note that at this case our calculation method will be no longer suitable because of the non-neglectable layer thickness of graphene). Therefore, another physical picture to understand this coupling of the multilayer graphene is that the multilayer-graphene-based structure can be seen as an indefinite metamaterial with hyperbolic dispersion relations.[44,45]

To further compare the resolution capabilities of the different multilayered graphene lenses, in Figure 5d,e, we use these lenses to image a 500-nm wide double slit with the separation of 1 μm at $f = 27.2$ THz (about a resolution of $\lambda/11$). It appears that the slits are well resolved for both cases. Also, consistent with our analysis, the performance of the 8-layered GL is better than that of the 4-layered case. Moreover, similar with the 2-layered case the effect of losses also does not obviously affect the performance of the multilayered lenses.

CONCLUSIONS

In summary, we have introduced a novel graphene-based device enabling the enhancement of evanescent waves for near-field subwavelength imaging. Owing to the nonresonant enhancement provided by the GSs, this GL yields new promising properties including broad intrinsic bandwidth and low sensitivity to loss, together with a still good subwavelength resolution of around $\lambda/7$ for a bilayer case and over $\lambda/10$ for the multilayered configuration. Most importantly, due to the large frequency-tunability *via* the dynamical tuning of chemical potentials, our proposed GL can act as an ultrabroadband subdiffraction-limited imaging device to in principle cover the nearly whole range from mid-IR to THz frequencies. Combining with the recent development of broadband light sources,[9,46] our lens would provide a real-time and large-area subdiffractive probing method for many spectroscopic applications, such as characterization of doping concentrations in semiconductors[7] and material identification.[8−10] We also notice the fact that layered graphene structures are commonly used in graphene electronics (like graphene transistors).[47] This does not only mean that the fabrication technology of such a GL is really mature, but also suggests that our concept may be directly useful for these electronic devices, such as for subsurface imaging of defects with the help of near-field microscopy.[39,40]

Besides these presented exciting results, the GL concept further offers other bright prospects: for example, a possibility is to roll the planar GL into a cylindrical shape, which may provide a tunable magnifying lens for far-field imaging at IR and THz frequencies. Moreover, since graphene is a two-dimensional (2D) conducting sheet, our concept of using conducting sheets for subwavelength imaging can also be generalized to that of a "conducting sheet lens" (CSL) and easily transferred to other conventional systems like 2D electron gases (2DEG), opening up various exciting ways to achieve broadband subwavelength imaging with semiconductor heterostructures.

METHODS

To calculate the OTF of layered GL, we use the transfer matrix method by treating GSs as ideal conducting sheets with surface conductivity σ_g. The characteristic matrix for the graphene can be obtained by using a mathematical trick similar with the process in ref 25. First, we suppose the graphene layer with the thickness Δ has the equivalent complex permittivity $\varepsilon_{eq} = \varepsilon_0 + i\sigma_g/(\omega\Delta)$. Then we employ this equivalent permittivity with the thickness Δ into the commonly used characteristic matrix[48] for layered systems and let $\Delta \to 0$. The thickness Δ will be canceled

in the formulas. Finally, we obtain the matrix of the graphene sheet as

$$M_g = \begin{bmatrix} 1 & \sigma_g/\varepsilon_0\omega \\ 0 & 1 \end{bmatrix} \quad (2)$$

With this characteristic matrix, it is easier to calculate the OTF of any multilayered GL.

We use a commercial software COMSOL based on the finite-element method to simulate the imaging performance of the GL. In the simulations, the graphene layer cannot be seen as the ideally thin sheet. So we assume that the thickness of graphene is 1 nm and use the corresponding permittivity ε_{eq}, taking into account the realistic surface conductivity of the graphene. For example, we obtain $\mathrm{Re}(\varepsilon_{eq}) \approx -720$ at the frequency $f = 27.2$ THz for the graphene layer with chemical potential $\mu_c = 1.5$ eV. Owing to the computation memory limitation introduced by the large mismatch between the ultrathin thickness and the long illuminating wavelength, the simulation is performed in two dimensions. The simulation domains have been assigned scattering properties following the same way as shown in ref 13, which act as the necessary open boundary conditions. For a workstation with 12-core CPUs (3.46 GHz) and 192 GB RAM memory, all the simulations with over 1 500 000 mesh cells reached proper convergence.

Conflict of Interest: The authors declare no competing financial interest.

Supporting Information Available: A discussion on the geometrical symmetry breaking shown in Figure 1a and determination of multiple modes of Fabry–Perot resonances. This material is available free of charge *via* the Internet at http://pubs.acs.org.

Acknowledgment. We thank the financial support from the Ministry of Innovation NRW and the German Excellence Initiative. We are grateful to B. Hauer, J. M. Hoffmann and Dr. T. Wang for valuable discussions and proofreading of the manuscript.

REFERENCES AND NOTES

1. Abbe, E. Beiträge zur Theorie des Mikroskops und der Mikroskopischen Wahrnehmung. *Arch. Mikroskop. Anat.* **1873**, *9*, 413–420.
2. Pendry, J. B. Negative Refraction Makes a Perfect Lens. *Phys. Rev. Lett.* **2000**, *85*, 3966–3969.
3. Zhang, X.; Liu, Z. Superlenses to Overcome the Diffraction Limit. *Nat. Mater.* **2008**, *7*, 435–441.
4. Lewis, A.; Taha, H.; Strinkovski, A.; Manevitch, A.; Khatchatourants, A.; Dekhter, R.; Ammann, E. Near-Field Optics: From Subwavelength Illumination to Nanometric Shadowing. *Nat. Biotechnol.* **2003**, *21*, 1378–1386.
5. Hartschuh, A. Tip-Enhanced Near-Field Optical Microscopy. *Angew. Chem., Int. Ed.* **2008**, *47*, 8178–8191.
6. Taubner, T.; Hillenbrand, R.; Keilmann, F. Nanoscale Polymer Recognition by Spectral Signature in Scattering Infrared Near-Field Microscopy. *Appl. Phys. Lett.* **2004**, *85*, 5064.
7. Huber, A. J.; Keilmann, F.; Wittborn, J.; Aizpurua, J.; Hillenbrand, R. Terahertz Near-Field Nanoscopy of Mobile Carriers in Single Semiconductor Nanodevices. *Nano Lett.* **2008**, *8*, 3766–3770.
8. Knoll, B.; Keilmann, F. Near-Field Probing of Vibrational Absorption for Chemical Microscopy. *Nature* **1999**, *399*, 134–137.
9. Huth, F.; Govyadinov, A.; Amarie, S.; Nuansing, W.; Keilmann, F.; Hillenbrand, R. Nano-FTIR Absorption Spectroscopy of Molecular Fingerprints at 20 nm Spatial Resolution. *Nano Lett.* **2012**, *12*, 3973–3978.
10. Brehm, M.; Taubner, T; Hillenbrand, R. Infrared Spectroscopic Mapping of Single Nanoparticles and Viruses at Nanoscale Resolution. *Nano Lett.* **2006**, *6*, 1307–1310.
11. Fang, N.; Lee, H. S.; Sun, C.; Zhang, X. Sub-diffraction Limited Optical Imaging with a Silver Superlens. *Science* **2005**, *308*, 534–537.
12. Taubner, T.; Korobkin, D.; Urzhumov, Y.; Shvets, G.; Hillenbrand, R. Near-Field Microscopy through a SiC Superlens. *Science* **2006**, *313*, 1595–1595.
13. Kehr, S. C.; Liu, Y. M.; Martin, L. W.; Yu, P.; Gajek, M.; Yang, S. -Y.; Yang, C. -H.; Wenzel, M. T.; Jacob, R.; von Ribbeck, H. -G.; *et al*. Near-field Examination of Perovskite-Based Superlenses and Superlens-Enhanced Probe-Object Coupling. *Nat. Commun.* **2011**, *2*, 249.
14. Kehr, S. C.; Liu, Y. M.; Martin, L. W.; Yu, P.; Gajek, M.; Yang, S. -Y.; Yang, C. -H.; Wenzel, M. T.; Jacob, R.; von Ribbeck, H. -G.; *et al*. Microspectroscopy on Perovskite-based Superlenses. *Opt. Mater. Express* **2011**, *1*, 1051–1060.
15. Li, P.; Taubner, T. Multi-wavelength Superlensing with Layered Phonon-Resonant Dielectrics. *Opt. Express* **2012**, *20*, 11787–11795.
16. Liu, H.; Wang, B.; Ke, L.; Deng, J.; Chum, C. C.; Teo, S. L.; Shen, L.; Maier, S. A.; Teng, J. H. High Aspect Subdiffraction-Limit Photolithography *via* a Silver Superlens. *Nano Lett.* **2012**, *12*, 1549–1554.
17. Jablan, M.; Buljan, H.; Soljačić, M. Plasmonics in Graphene at Infrared Frequencies. *Phys. Rev. B* **2009**, *80*, 245435.
18. Fei, Z.; Andreev, G. O.; Bao, W.; Zhang, L. M.; McLoed, A. S.; Wang, C.; Stewart, M. K.; Zhao, Z.; Dominguez, G.; Thiemens, M.; *et al*. Infrared Nanoscopy of Dirac Plasmons at the Graphene–SiO_2 Interface. *Nano Lett.* **2011**, *11*, 4701–4705.
19. Chen, J.; Badioli, M.; Alonso-González, P.; Thongrattanasiri, S.; Huth, F.; Osmond, J.; Spasenović, M.; Centeno, A.; Pesquera, A.; Godgnon, P.; *et al*. Optical Nano-imaging of Gate-Tunable Graphene Plasmons. *Nature* **2012**, *487*, 77–81.
20. Fei, Z.; Rodin, A. S.; Andreev, G. O.; Bao, W.; McLoed, A. S.; Wagner, M.; Zhang, L. M.; Zhao, Z.; Thiemens, M.; Dominguez, G.; *et al*. Gate-Tuning of Graphene Plasmons Revealed by Infrared Nano-imaging. *Nature* **2012**, *487*, 82–85.
21. Koppens, F. H. L.; Chang, D. E.; García de Abajo, F. J. Graphene Plasmonics: A Platform for Strong Light–Matter Interactions. *Nano Lett.* **2011**, *11*, 3370–3377.
22. Christensen, J.; Manjavacas, A.; Thongrattanasiri, S.; Koppens, F. H. L.; García de Abajo, F. J. Graphene Plasmon Waveguiding and Hybridization in Individual and Paired Nanoribbons. *ACS Nano* **2012**, *6*, 431–440.
23. Bao, Q.; Zhang, H.; Wang, B.; Ni, Z.; Lim, C. H. Y. X.; Wang, Y.; Tang, D. Y.; Loh, K. P. Broadband Graphene Polarizer. *Nat. Photon.* **2011**, *5*, 411–415.
24. Stauber, T.; Gómez-Santos, G. Plasmons and Near-field Amplification in Double-Layer Graphene. *Phys. Rev. B* **2011**, *85*, 075410.
25. Vakil, A.; Engheta, N. Transformation Optics Using Graphene. *Science* **2011**, *332*, 1291–1294.
26. Ju, L.; Geng, B.; Horng, J.; Girit, C.; Martin, M.; Hao, Z.; Bechtel, H. A.; Liang, X.; Zettl, A.; Shen, Y. R.; *et al*. Graphene Plasmonics for Tunable Terahertz Metamaterials. *Nat. Nanotechnol.* **2011**, *6*, 630–634.
27. Papasimakis, N.; Luo, Z.; Shen, Z. X.; Angelis, F. D.; Fabrizio, E.; Nikolaenko, A. E.; Zheludev, N. Graphene in a Photonic Metamaterial. *Opt. Express* **2010**, *18*, 8353–8359.
28. Chen, P.-Y.; Alù, A. Atomically Thin Surface Cloak Using Graphene Monolayers. *ACS Nano* **2011**, *5*, 5855–5863.
29. Wang, J.; Xu, Y.; Chen, H. Ultraviolet Dielectric Hyperlens with Layered Graphene and Boron Nitride. *J. Mater. Chem.* **2012**, *22*, 15863–15868.
30. Fang, Z.; Liu, Z.; Wang, Y.; Ajayan, P. M.; Nordlander, P.; Halas, N. J. Graphene-Antenna Sandwich Photodetector. *Nano Lett.* **2012**, 3808–3813.
31. Wang, F.; Zhang, Y.; Tian, C.; Girit, C.; Zettl, A.; Crommie, M.; Shen, Y. R. Gate-Variable Optical Transitions in Graphene. *Science* **2008**, *320*, 206–209.
32. Horng, J.; Chen, C.; Geng, B.; Girit, C.; Zhang, Y.; Hao, Z.; Bechtel, H. A.; Martin, M.; Zettl, A.; Crommie, M.; *et al*. Drude Conductivity of Dirac Fermions in Graphene. *Phys. Rev. B* **2011**, *83*, 165113.
33. Li, Z. Q.; Henriksen, E. A.; Jiang, Z.; Hao, Z.; Martin, M. C.; Kim, P. Stormer, H. L.; Basov, D. N. Dirac Charge Dynamics in Graphene by Infrared Spectroscopy. *Nat. Phys.* **2008**, *4*, 532–535.
34. Falkovsky, L.; Pershoguba, S. Optical Far-infrared Properties of a Graphene Monolayer and Multilayer. *Phys. Rev. B* **2007**, *76*, 153410.

35. Gan, C. H.; Chu, H. S.; Li, E. P. Synthesis of Highly Confined Surface Plasmon Modes with Doped Graphene Sheets in the Midinfrared and Terahertz Frequencies. *Phys. Rev. B* **2012**, *85*, 125431.
36. Solymar, L.; Shamonina, E. *Waves in Metamaterials*; Oxford University Press: New York, 2009.
37. Mann, D.; Javey, A.; Kong, J.; Wang, Q. Ballistic Transport in Metallic Nanotubes with Reliable Pd Ohmic Contacts. *Nano Lett.* **2003**, *3*, 1541–1544.
38. Wood, B.; Pendry, J.; Tsai, D. P. Directed Subwavelength Imaging Using a Layered Metal-Dielectric System. *Phys. Rev. B* **2006**, *74*, 115116.
39. Taubner, T.; Keilmann, F.; Hillenbrand, R. Nanoscale-Resolved Subsurface Imaging by Scattering-Type Near-Field Optical Microscopy. *Opt. Express* **2005**, *13*, 8893–8899.
40. Hauer, B.; Engelhardt, A. P.; Taubner, T. Quasi-analytical Model for Scattering Infrared Near-Field Microscopy on Layered Systems. *Opt. Express* **2012**, *20*, 13173–13188.
41. Ramakrishna, S. A.; Pendry, J. B.; Schurig, D.; Smith, D. R.; Schultz, S. The Asymmetric Lossy Near-Perfect Lens. *J. Mod. Opt.* **2002**, *49*, 1747–1762.
42. Ye, J.; Craciun, M. F.; Koshino, M.; Russo, S.; Inoue, S.; Yuan, H.; Shimotani, H.; Morpurgo, A. F.; Iwasa, Y. Accessing the Transport Properties of Graphene and Its Multilayers at High Carrier Density. *Proc. Natl Acad. Sci. U.S.A.* **2011**, *108*, 13002–13006.
43. Efetov, D.; Kim, P. Controlling Electron-Phonon Interactions in Graphene at Ultrahigh Carrier Densities. *Phys. Rev. Lett.* **2010**, *105*, 256805.
44. Smith, D. R.; Schurig, D. Electromagnetic Wave Propagation in Media with Indefinite Permittivity and Permeability Tensors. *Phys. Rev. Lett.* **2003**, *90*, 077405.
45. Fang, A.; Koschny, T.; Soukoulis, C. M. Optical Anisotropic Metamaterials: Negative Refraction and Focusing. *Phys. Rev. B* **2009**, *79*, 245127.
46. Amarie, S.; Keilmann, F. Broadband-Infrared Assessment of Phonon Resonance in Scattering-Type Near-Field Microscopy. *Phys. Rev. B* **2011**, *83*, 045404.
47. Schwierz, F. Graphene Transistors. *Nat. Nanotechnol.* **2010**, *5*, 487–496.
48. Born, M.; Wolf, E. *Principles of Optics*; Cambridge University Press: Cambridge, 1999.